Supporting Information

Iron single-atom site on MXene for a high-performance interdigitated micro-supercapacitor

Mariyarathinam Vinoth Inbaraj, [a] Mohandas Sanjay Kumar,[b] Muthuramalingam Prakash,[b,c] and Govindhan Maduraiveeran*[a,d]

[a] Materials Electrochemistry Laboratory, Department of Chemistry, SRM Institute of Science and Technology, Kattankulathur - 603 203, Chengalpattu, Tamil Nadu, India

[b] Computational Chemistry Research Laboratory (CCRL), Department of Chemistry, SRM Institute of Science and Technology, Kattankulathur-603 203, Tamil Nadu, India

[c] Centre for Advanced Computational and Theoretical Sciences (ACTS), SRM Institute of Science and Technology, Kattankulathur-603 203, Tamil Nadu, India

[d] Materials Research Center, American University of Sharjah, Sharjah - 26666, UAE

**Corresponding Author: mgovindhan@aus.edu & pgmadura@yahoo.co.in*

Experimental section:

Materials

Potassium hydroxide (KOH) and acetone were received from SRL Pvt. Ltd., Maharashtra, India. Sulphuric acid was purchased from RANKEM, Maharashtra, India. Ethanol received from Hayman, Witham, UK. Poly Vinyl Alcohol, Carbon black, activated carbon, and MAX phase (Ti_3AlC_2) were received from Otto Kemi, Maharashtra, India. Hydrofluoric acid, Nafion, and commercial carbon fiber microelectrodes (diameter: ~300 μm) with a purity of 99.99% were acquired from Sigma Aldrich, USA. The carbon microfiber (CMF) was washed several times with deionized water and then ultrasonically treated with a 1:1 ethanol-to-acetone ratio for a short time. The CMF was then dried completely at 50 °C. The pretreatment is followed by further analysis using the CMF. All of the chemicals were analytical grade and were used straight without further purification.

Synthesis of MXene

Using the HF etching method, MXene (TiC_2T_x) has been produced by selectively etching the aluminium layer from the Ti_3AlC_2 MAX phase. A standard process involves adding 1.0 gram of Ti_3AlC_2 powder, gradually added to 20 ml of 40% hydrofluoric acid in a Teflon container inside a fume hood. The mixture is stirred at room temperature for 24 hours to ensure complete etching of the Al layers. After etching, the product is centrifuged several times with deionized water at 2500-3000 rpm until the pH of the supernatant reaches around~6.0. Then, the sediment is dried at 50°C for 24 hours. The resulting sediment contains multilayered MXene ($Ti_3C_2T_x$).

Electrochemical augmentation process of CMF-200

The pretreated pristine CMF-200 microelectrode with a geometrical surface area of ~0.096 cm^2 (a radius of ~150 μm and a height of ~10 mm) was immersed in 3.0 M KOH. The cyclic voltammograms (CV) of the CMF electrodes were recorded in the operating potential range,

starting from -0.2 V to +0.8 V (vs. Ag/AgCl) at a scan rate of 10 mV s^{-1} for 200 continuous cycles. The as-developed electrodes were used to perform the micro-supercapacitor (MSC) studies.[1]

MXene-CMF electrode preparation

Initially, 4.0 mg of $Ti_3C_2T_x$ MXene powder is dispersed in a minimal amount of deionized water using mild sonication. Then, 0.5 mg of activated carbon and 0.5 mg of carbon black are added to the MXene dispersion to enhance the conductivity of the ink. After thorough mixing, 50 µL of 1% Nafion solution is introduced as a binder to improve adhesion. The mixture is sonicated or stirred vigorously for ten minutes until a homogeneous, stable ink is obtained. Then the electrochemically augmented carbon microfiber electrodes were dipped directly into the MXene conductive ink, and then they dried overnight at 50°C. The obtained electrodes are called MXene-CMF electrodes.

Electrodeposition of Fe SAS to MXene-CMF electrode

To place Fe single atoms onto the prepared MXene-based electrode, an electrolyte solution is first prepared by dissolving 100 µM of $FeCl_3$ in anhydrous N, N-dimethylformamide (DMF). This solution is sonicated for 60 minutes to ensure complete dissolution and uniform dispersion of Fe^{3+} ions. After sonication, the MXene-CMF-based electrode is used as the working electrode in a standard three-electrode electrochemical cell, with a platinum wire as the counter electrode and an Ag/AgCl as the reference electrode. The electrochemical deposition is carried out using cyclic voltammetry at a controlled potential suitable for Fe^{3+} reduction. Typically, ~-1.2 to 0.6 V. The deposition cycle is carefully optimized to ensure single-atom dispersion, preventing the formation of Fe clusters or nanoparticles. After deposition, the electrode is gently rinsed with water and dried under vacuum overnight.

Fabrication of an interdigitated micro-supercapacitor device

Primarily, to prepare the gel electrolyte, 1.0 g of polyvinyl alcohol (PVA) was mixed with 10 mL of deionized water. The above mixture was heated to 60°C, and 10 mL of 1.0 M H_2SO_4 was added slowly under vigorous stirring until the mixture became clear. After coating the polyethylene sheet (1.0 cm^2) with the gel, the ~7.0 mm Fe SAS-MXene-CMF and two current collectors (~15 mm) were immersed in it. After that, they were all left to gelatinize at room temperature (26 ±1°C) for 3 min. Again, the electrodes and current collectors were dipped in gel electrolyte and assembled in the interdigitated shape with a space of ~2 mm on the sheet. They were then covered with gel electrolyte, which was then left to fix at room temperature for 24 h.

Surface characterization

The surface morphology and elemental composition were investigated using high-resolution scanning electron microscopy (HR-SEM, FEI QUANTA 200). Transmission electron microscopic (TEM) and high-resolution transmission electron microscopic (HRTEM) studies were conducted with a JEOL 2010F TEM. The functional groups were identified using FT-IR spectroscopy, a SHIMADZU, IRTRACERR 100. To study the X-ray diffraction (XRD) patterns, a PAN analytical Xpert Pro diffractometer with a monochromatic Cu Kr (1.5406, 2.2 KW Max) filter was used. X-ray photoelectron spectroscopy (XPS) (XPS-PHI Versa probe III) was used to investigate the chemical state and chemical composition analysis of the electrodes.

Electrochemical measurements

Cyclic voltametric studies were performed to understand the electrochemical characteristics of the Fe-SA-MXene-CMF electrodes using the Metrohm Autolab B.V. workstation (AUT204). The electrochemical impedance spectroscopy (EIS), cycling stability test, and galvanostatic

charge-discharge (GCD) methods were conducted with an OrigaLys multichannel system (Origaflex OGF500) workstation at the open-circuit potential without bias potential. Electrochemical experiments were conducted at room temperature in 1.0 M H_2SO_4 electrolyte. CV studies were performed at various scan rates, starting from 10 to 60 mV s^{-1}, and GCD results were conducted with current densities from 0.5 to 2.0 mA cm^{-2} and a potential from 0 to 0.6 V (Ag/AgCl). The EIS measurement's frequency range and AC amplitude were set from 1 kHz to 100 mHz at open-circuit potential in 1.0 M H_2SO_4.

Calculation method

In this study, the electrochemical tests were conducted based on defined area ratio parameters. The measured areal capacitance, along with the calculated areal energy and power densities, reflects the performance characteristics of the flexible all-solid-state micro-supercapacitors. The areal capacitance of individual electrodes was determined using the Equations (1) and (2) from galvanostatic charge discharge (GCD) and CV data[2], respectively. Equation (3) was used to calculate the areal capacitance of the full device, while Equations (4) and (5) were applied to estimate the corresponding areal energy and power densities[3,4].

$$\mathrm{A.C_{(Electrode)}} = \frac{2\mathrm{I} \times \Delta\mathrm{t}}{\Delta V} \qquad (1)$$

$$A.C_{(Electrode)} = \frac{\int IdV}{v \times A \times \Delta V} \qquad (2)$$

$$\mathrm{A.C_{(Device)}} = \frac{\mathrm{I} \times \Delta\mathrm{t}}{\Delta V} \qquad (3)$$

$$\mathrm{E_{(Device)}} = \frac{A.C_{(Device)} \times \Delta V^2}{2} \qquad (4)$$

$$P_{(Device)} = \frac{E_{(Device)}}{\Delta\mathrm{t}} \qquad (5)$$

Where A.C represents the areal capacitance; E and P mean the energy and power densities of the device; I represents the current density of charge and discharge; $\int IdV$ represents the

absolute area; v represents the scan rate; ΔV represents the potential window; and Δt is the discharge time.

The electrochemically active surface area (ECSA) of the electrodes was calculated using the double layer capacitance (C_{dl}) and specific capacitance C_s (3293 μF cm^{-2}) using Eqn. 6.

$$ECSA = \frac{C_{dl}}{C_s} \qquad (6)$$

Additionally, using Eqn. (7), the roughness factor (RF) of the electrodes can be calculated using ECSA and geometrical surface area (GSA).

$$RF = \frac{ECSA}{GSA} \qquad (7)$$

The Coulombic efficiency (η) of the SSC-200|CMF and AI-MSCs was calculated from the GCD curve using Eqn. (8). where t_c and t_d represent the charge and discharge times, respectively.

$$\eta = \frac{t_d}{t_c} \times 100\ \% \qquad (8)$$

$$i(V) = k_1 V + k_2 V^{0.5} \qquad (9)$$

The overall capacitive and diffusive contribution is evaluated by using the Dunn method equation (Eqn. (9)). i(V) is the total current measured at a particular voltage (V) in the CV, and (k_1V) is the capacitive contribution, and $k_2V^{0.5}$, is the diffusive contribution[5,6].

DFT studies:

All periodic DFT calculations were performed using the CP2K program package (Quickstep module), which employs a hybrid Gaussian and plane-wave (GPW) formalism. The PBE generalized gradient approximation (GGA) exchange-correlation functional was used to describe the electronic structure of the system.[7] Long-range dispersion interactions were accounted for using the DFT-D3 scheme with Becke-Johnson damping, as implemented in

CP2K.[8] The core–valence interactions were described using Goedecker-Teter-Hutter (GTH) norm-conserving pseudopotentials, while the valence electronic wave functions were expanded in Gaussian basis sets of the MOLOPT family.[9] Specifically, TZVP-MOLOPT-GTH basis sets were employed for C and O atoms, while DZVP-MOLOPT-SR-GTH basis sets were used for Ti and Fe atoms. A plane-wave cutoff energy of 450 Ry and a relative cutoff of 50 Ry were used to ensure the convergence of the total energy and forces. The Brillouin zone was sampled at the Γ point due to the large size of the unit cell. Spin-polarized (UKS) calculations were performed. Structural optimizations were carried out using the BFGS algorithm for both atomic positions and cell parameters (CELL_OPT run type).[10] The convergence criteria for geometry optimization were set to a maximum force of 1×10^{-3} Ha/Bohr, an RMS force of 1×10^{-4} Ha/Bohr, and maximum and RMS displacements of 0.005 Å and 0.0025 Å, respectively. A maximum of 1000 optimization steps was allowed. The self-consistent field (SCF) cycles employed the orbital transformation (OT) method with a conjugate gradient minimizer, using an energy gap of 0.001 Ha. The convergence threshold for the SCF loop was set to 10^{-7} Ha.S The adsorption energy of the Fe atom on $Ti_3C_2O_3$ was evaluated using the following Eqn. (10).[11]

$$E_{ads} = E_{(Fe@Ti_3C_2X_3)} - (E_{Ti_3C_2X_3} + E_{Fe}) \qquad (10)$$

Where E(Fe@ $Ti_3C_2X_3$), E($Ti_3C_2X_3$), and E(Fe) represent the total energies of the Fe-adsorbed $Ti_3C_2X_3$ composite, the pristine $Ti_3C_2X_3$ surface, and the isolated Fe atom, respectively. A more negative E_{ads} value indicates stronger adsorption. To further understand the thermodynamic stability and dynamics of the Fe-adsorbed $Ti_3C_2O_3$ system at finite temperature, *ab initio* molecular dynamics (AIMD) simulations were performed using the NVT ensemble. The temperature was maintained at 300 K using a Nosé–Hoover thermostat. Each trajectory was propagated for 4000 steps with a time step of 1 fs, corresponding to a total simulation time of 4 ps. The MD simulations employed the same computational parameters, basis sets,

pseudopotentials, and energy cutoffs as those used in the static DFT calculations to ensure consistency. The obtained trajectories were subsequently analysed to evaluate the structural stability, bonding interactions, and thermal fluctuations of the Fe@$Ti_3C_2O_3$ composite.

Density Functional Theory Results

To investigate the possibility of stabilizing Fe single atoms on oxygen- and fluorine-terminated Ti_3C_2 MXene surfaces, density functional theory (DFT) calculations were performed. The O- and F-terminated Ti_3C_2 surfaces offer several potential adsorption sites for anchoring metal atoms, including the hollow site of carbon, the hollow site of titanium, and the top site of oxygen, as illustrated in **Fig. S21** Structural optimizations revealed that the Fe atom preferentially adsorbs at the site coordinated by three surface oxygen atoms, forming strong Fe–O bonds that significantly stabilize the single-atom configuration. In contrast, on the F-terminated surface, the Fe atom tends to reside near the Ti–F region, forming weaker interactions. For the O-terminated Ti_3C_2 MXene, the adsorption energies at the three considered sites (A, B, and C) were -2.11, -2.32, and -2.62 eV, respectively, while the corresponding values for the F-terminated surface were -1.34, -1.71, and -1.77 eV. Among the two terminations, the O-terminated MXene exhibits stronger adsorption strength, with the most stable configuration (Fe coordinated with three neighbouring O atoms at the hollow site above Ti) showing an adsorption energy of -2.62 eV. This adsorption energy indicates a strong binding interaction between Fe and the O-terminated MXene surface. In contrast, the weaker adsorption at other sites suggests that Fe atoms spontaneously migrate toward the tri-oxygen coordination environment during relaxation. The strong Fe-O binding implies that Fe atoms are unlikely to aggregate or diffuse, thereby fulfilling a key stability criterion for single-atom catalysts.

To further assess the potential for Fe incorporation into the MXene lattice, substitutional doping of Fe at Ti sites was investigated. The calculated formation energy for this process was

found to be substantially high, indicating that Fe substitution for Ti is thermodynamically unfavourable under equilibrium conditions. Therefore, surface anchoring is identified as the preferred stabilization mode. The optimized structure of the most stable configuration exhibits an average Fe-O bond length of 1.94 Å, which is consistent with reported Fe-O coordination distances in oxide-supported single-atom catalysts, confirming a robust metal–support interaction. The thermal and dynamic stability of the Fe single-atom configuration was further verified using ab initio molecular dynamics (AIMD) simulations at 300 K. Throughout the simulation, the Fe atom remained firmly anchored to the O-terminated surface without detachment or migration. The Fe-O bond distances exhibited only minor fluctuations, indicating the absence of significant structural distortions. This confirms that the Fe single-atom site is thermally stable and maintains its local coordination environment under realistic conditions. **Fig. S22** illustrates the structural stability of Fe on the O-terminated Ti_3C_2 surface. Overall, these findings demonstrate that Fe can be effectively stabilized as a single atom on the O-terminated Ti_3C_2 MXene surface through strong Fe-O interactions, providing a promising foundation for the development of Fe-based single-atom catalysts supported on MXene.

Table S1. Comparison of areal capacitance of the developed electrodes in this study with different applied current densities.

S. No	Current Density ($mA\ cm^{-2}$)	CMF ($mF\ cm^{-2}$)	MXene ($mF\ cm^{-2}$)	Fe-SA-MXene ($mF\ cm^{-2}$)
1	0.5	6.65	471	869
2	1.0	5.95	450	845
3	1.5	5.82	428	812
4	2.0	5.80	415	786

Table S2. Comparison of areal capacitance, energy and power densities of the Fe-SA-MXene-MSCs device with different applied current densities.

S. No	Current Density (mA cm^{-2})	Areal Capacitance (mF cm^{-2})	Energy Density (µWh cm^{-2})	Power Density (µW cm^{-2})
1	0.8	24.6	1.23	40.9
2	1.0	23.9	1.19	50.8
3	1.2	22.7	1.13	59.9
4	1.4	21.6	1.08	68.7
5	1.6	21.5	1.07	80.7
6	1.8	20.7	1.03	89.7
7	2.0	20.4	1.02	102.31

Table S3. Comparison of the supercapacitance performance of the recent MXene-based electrode materials.

S. No	Material	Areal Capacitance (mF cm^{-2})	Energy Density (µWh cm^{-2})	Power Density (µW cm^{-2})	Capacitance Retention (%)	Stability Cycles	Ref.
1	Heterogeneous MXene/PEDOT:PSS	5.7	0.36	1.08	95	10000	Ref.[12]
2	Clay like Ti_3C_2 MXene	25	0.77	46.6	92	10000	Ref.[13]
3	3D-MXene rGO aerogel	34.6	2.18	60	91	15000	Ref.[14]
4	Ti_3C_2 MXene Thin film	12.5	2.48	0.16	100	100	Ref.[15]
5	2D-MXene	23	-	7.8	95	10000	Ref.[16]
6	Ti_3C_2Tx MXene	2.58	170	13	97.7	10000	Ref.[17]
7	M@O-CF//MnO_2/CNTs	1130.1	818	-	81.8	5000	Ref.[18]
8	WL-M-AE	483	109	1070	84.1	1000	Ref.[19]
9	**Fe-SA-MXene**	**24.6**	**1.23**	**40.9**	**95.4**	**5000**	**This Work**

PEDOT: PSS- Poly (3,4-ethylenedioxythiophene) polystyrene sulfonate; M@O-CF//MnO_2/CNTs- Oxygen plasma-activated carbon felt and MXene nanosheets paired with MnO_2 nanowires/carbon nanotube; WL-M-AE- Wood-like MXene aerogel electrode.

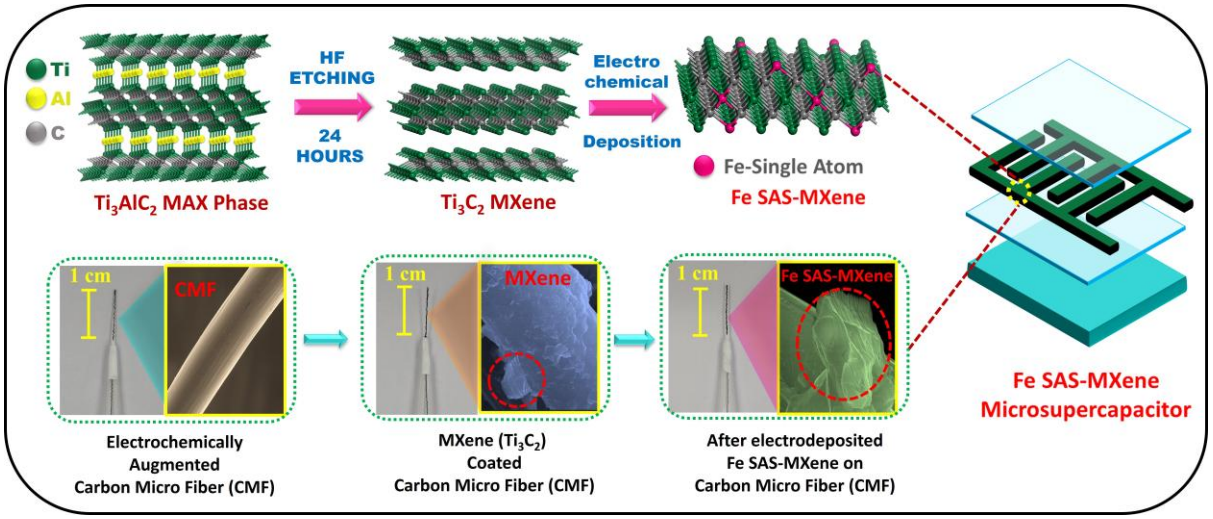

Fig. S1. Schematic illustration for the fabrication process of MXene and Fe SAS-MXene electrodes and their integration into an interdigitated micro-supercapacitor device.

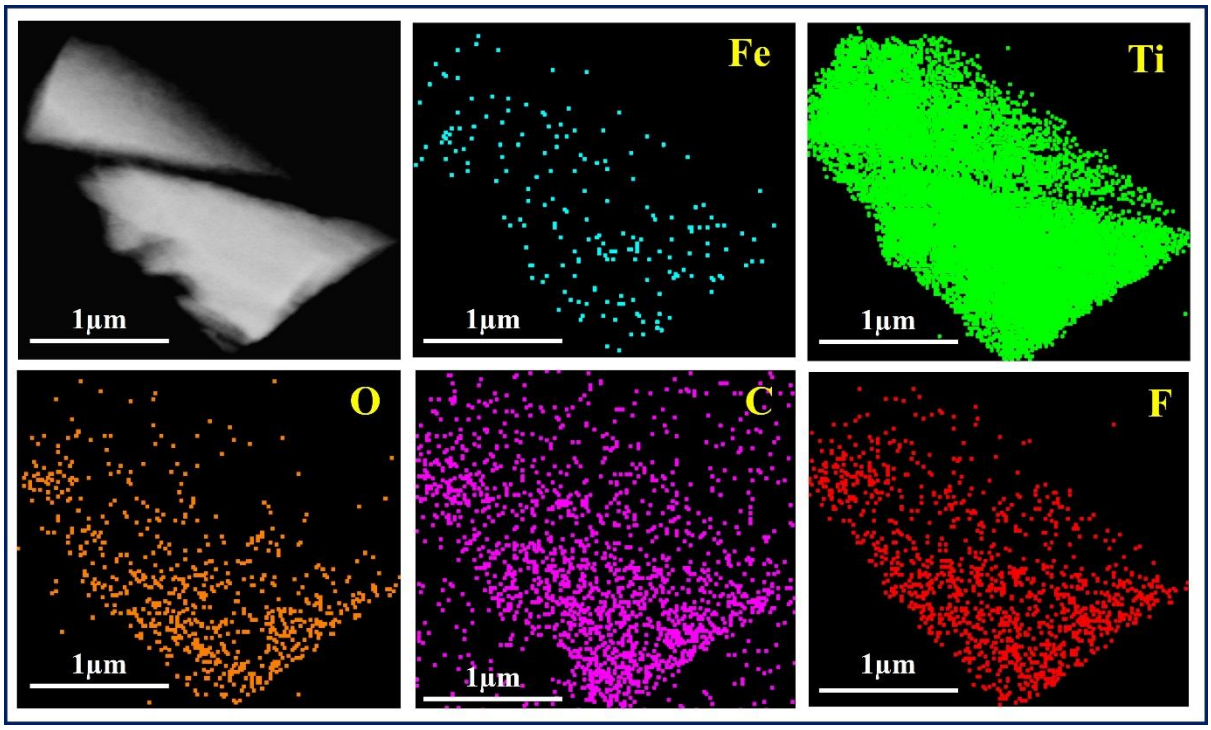

Fig. S2. TEM elemental mapping (Fe, Ti, O, C, and F) of the Fe SAS-MXene electrode.

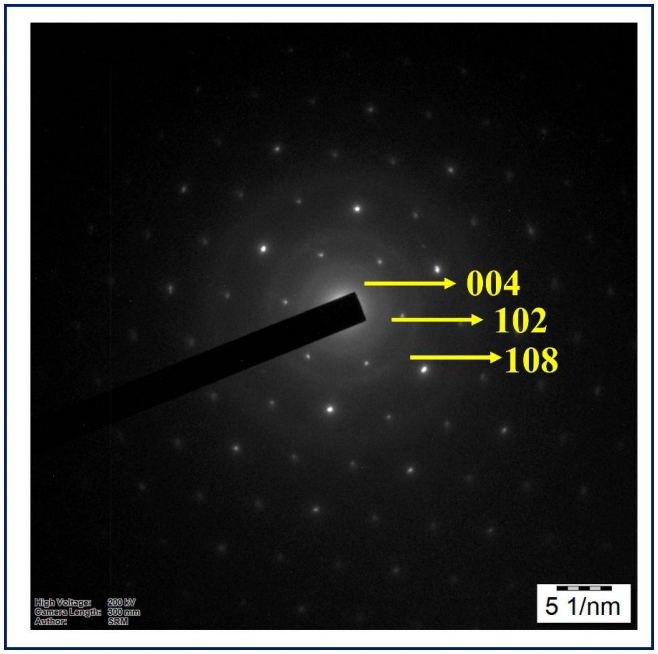

Fig. S3. SAED pattern of the Fe SAS-MXene.

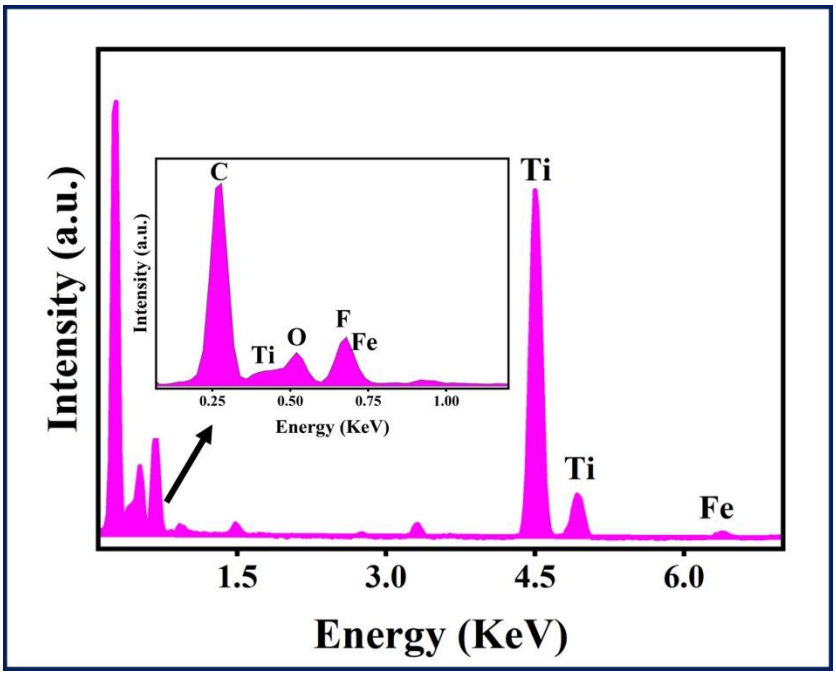

Fig. S4. EDS spectra of the Fe SAS-MXene.

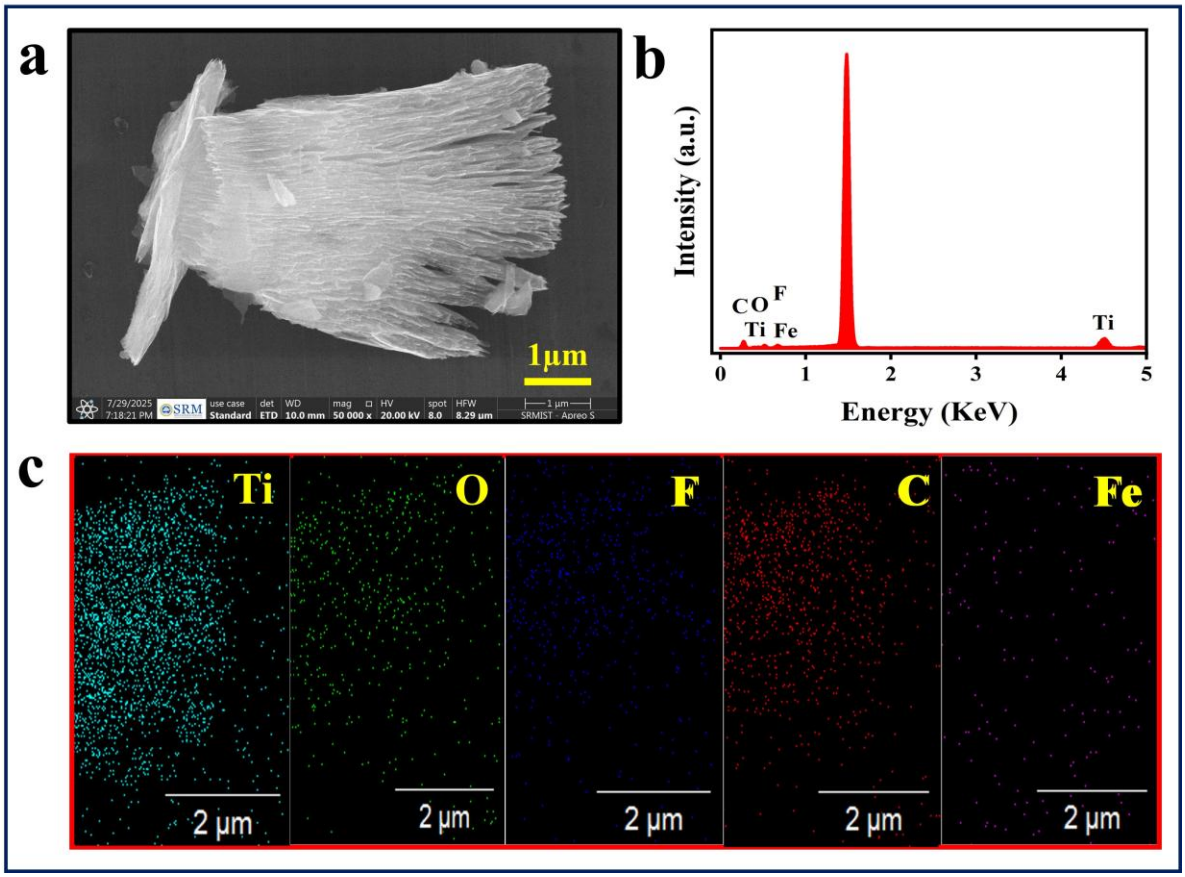

Fig. S5. SEM image **(a),** EDX spectra **(b),** and the elemental mapping **(c)** (Ti, C, O, F, and Fe) of the Fe SAS-MXene.

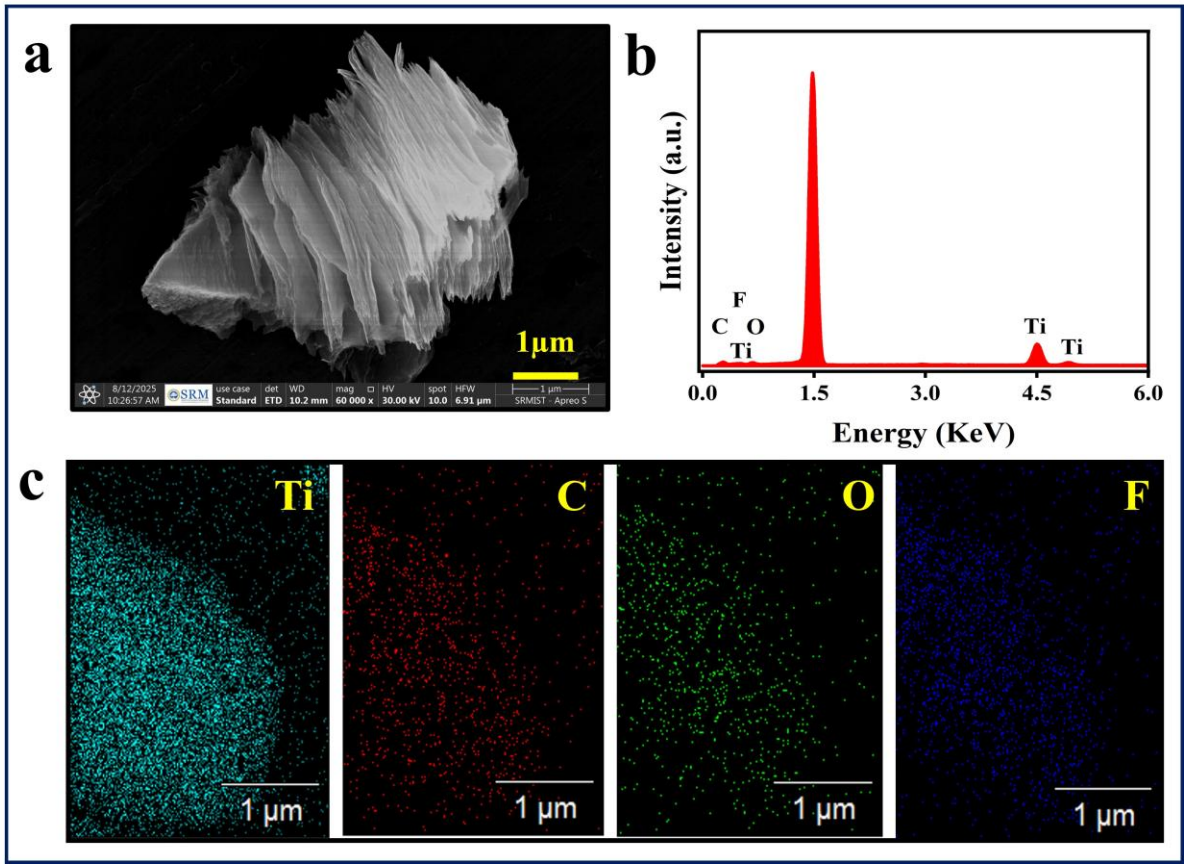

Fig. S6: SEM image **(a),** EDX spectra **(b),** and elemental mapping **(c)** (Ti, C, O, and F) of MXene.

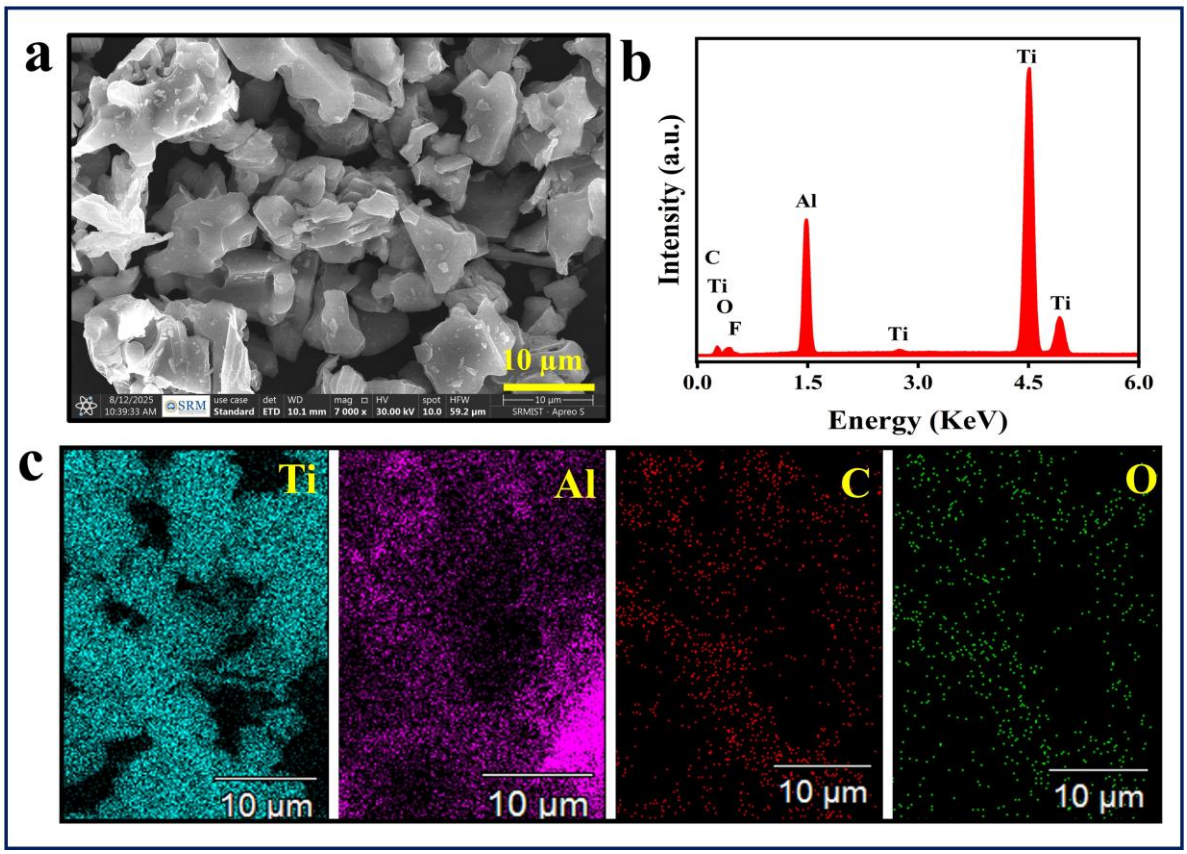

Fig. S7. SEM image **(a),** EDX spectrum **(b),** and elemental mapping **(c)** (Ti, Al, C, O, and F) of MAX phase Ti_3AlC_2.

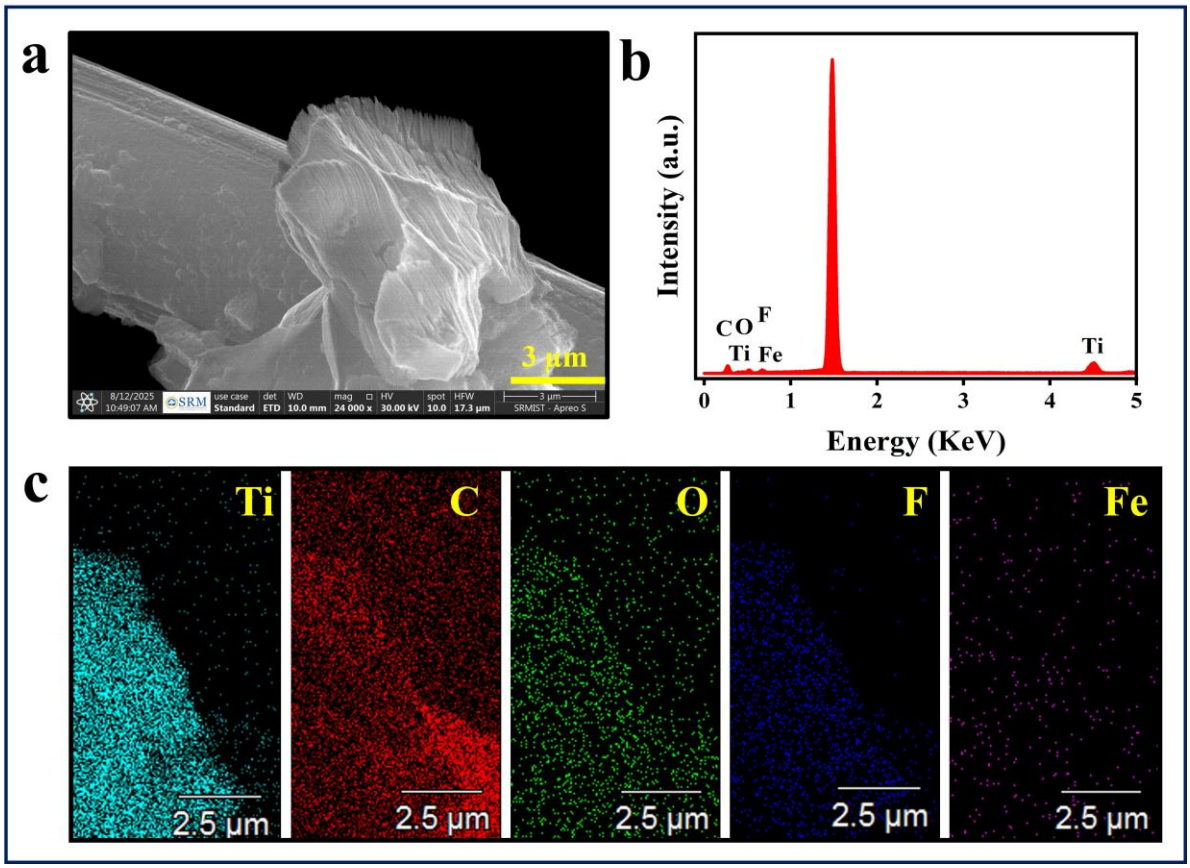

Fig. S8: SEM image **(a),** EDX spectrum **(b),** and elemental mapping **(c)** (Ti, C, O, F, Fe) of Fe SAS-MXene with CMF.

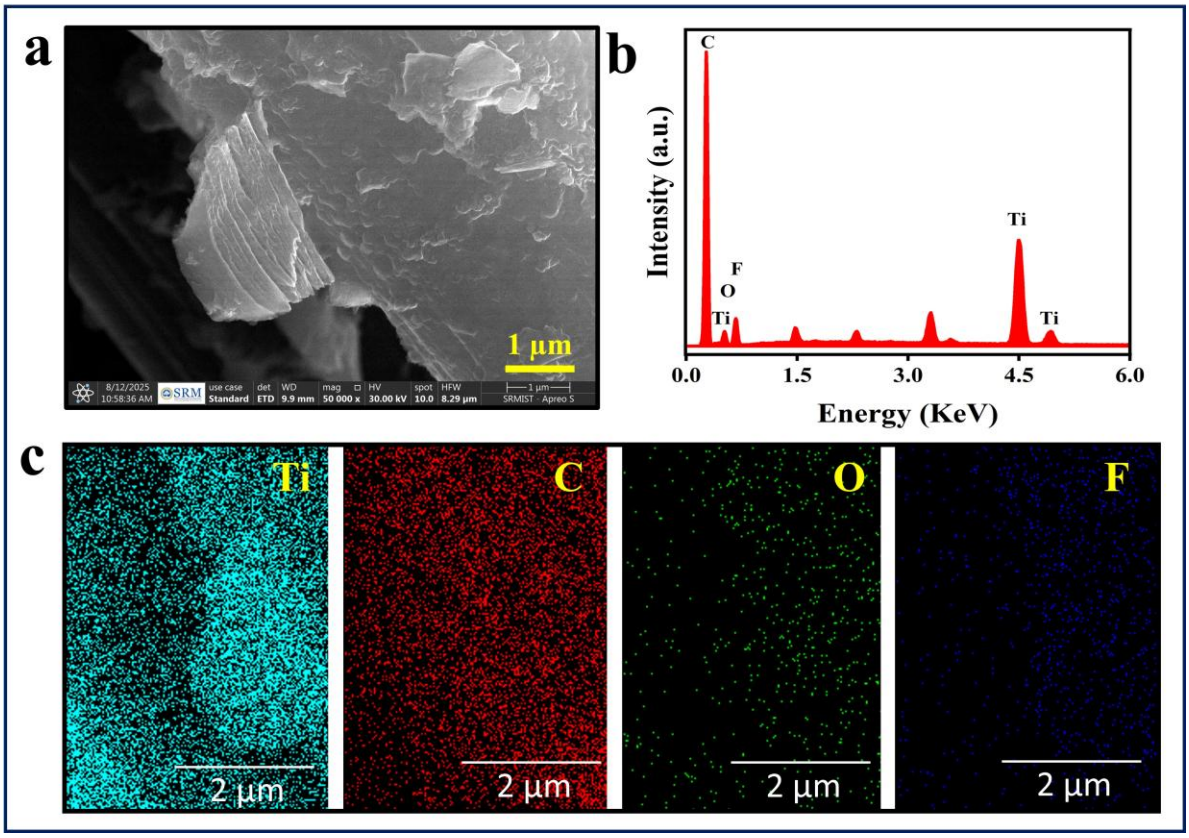

Fig. S9. SEM image **(a),** EDX spectrum **(b),** and elemental mapping **(c)** (Ti, C, O, and F) of MXene with CMF.

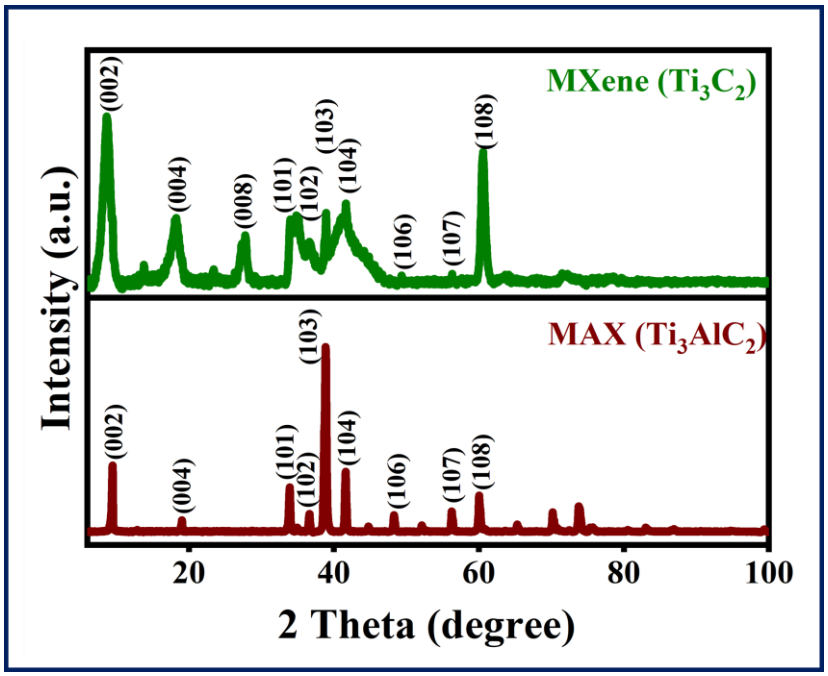

Fig. S10. XRD pattern comparison of MAX phase Ti_3AlC_2 (brown) and MXene (green).

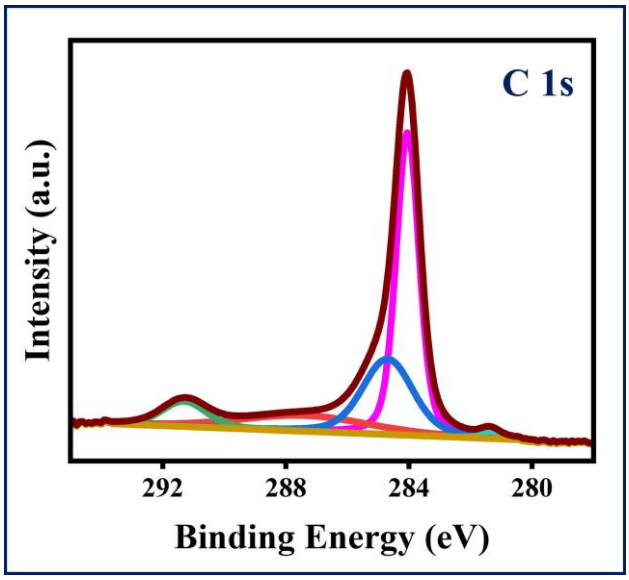

Fig. S11. XPS C 1s spectra for Fe SAS-MXene electrodes.

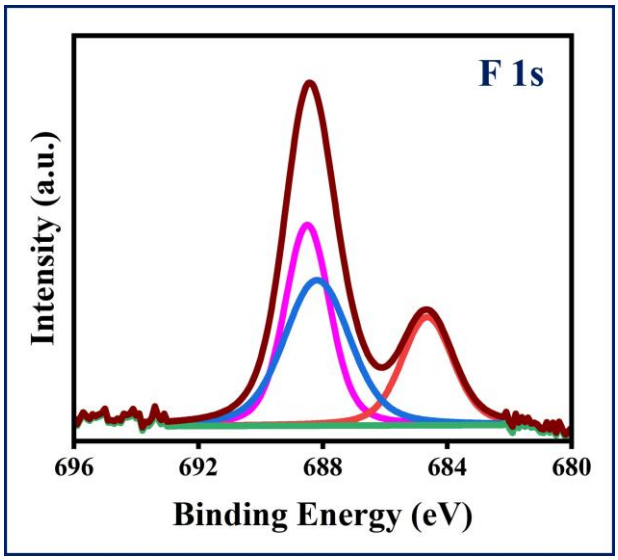

Fig. S12. XPS F 1s spectra for Fe SAS-MXene electrode.

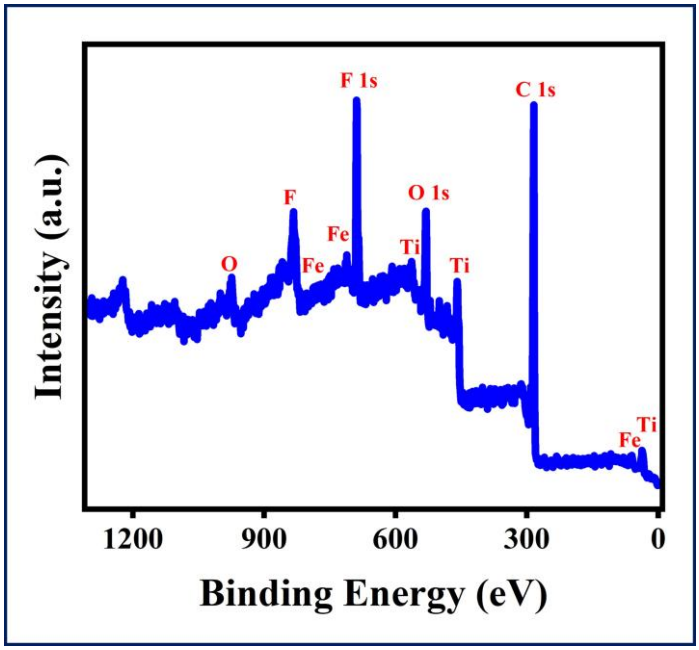

Fig. S13. XPS survey spectra of the Fe SAS-MXene electrode.

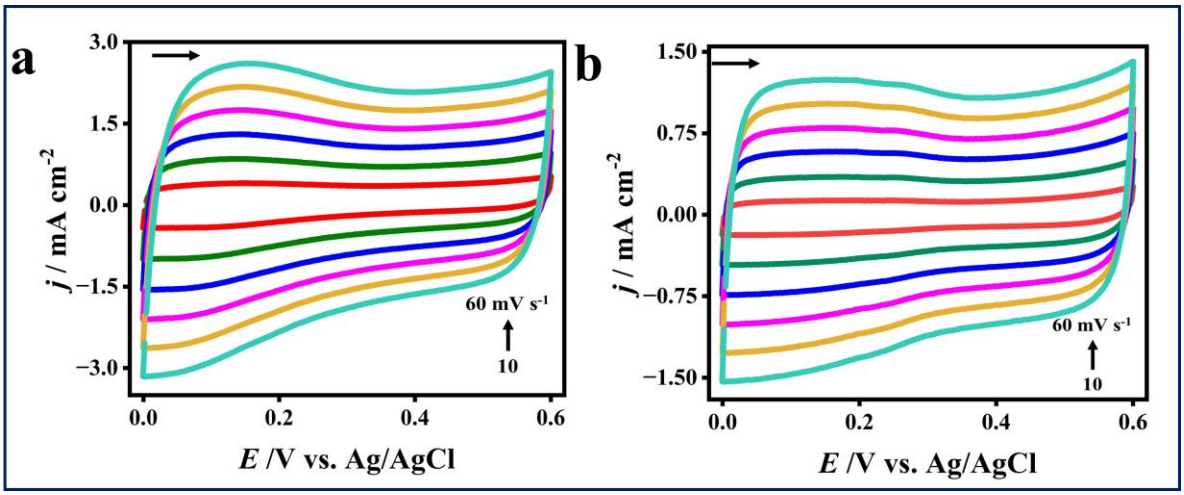

Fig. S14. CV curves of Fe SAS-MXene **(a),** and MXene electrodes **(b)** under 1.0 M H_2SO_4 at the various scan rates, starting from 10 to 60 mV s^{-1}.

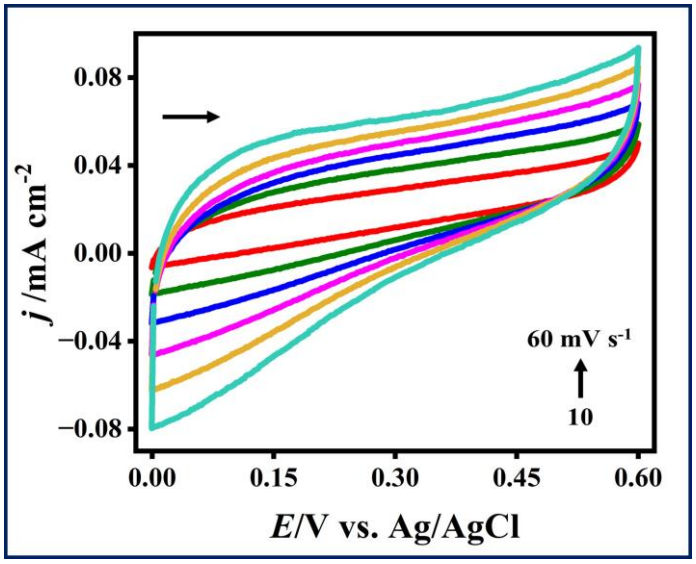

Fig. S15: CV curves of the CMF-200 electrode under 1.0 M H_2SO_4 at the various scan rates, starting from 10 to 60 mV s^{-1}.

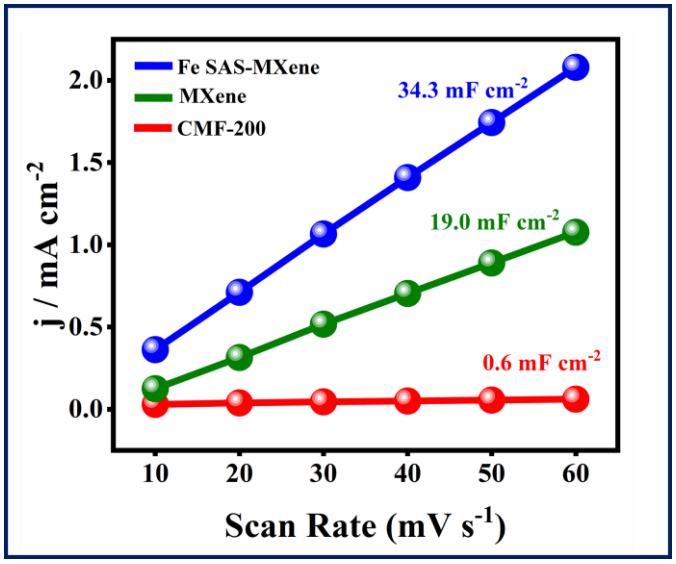

Fig. S16. ECSA plot of the CMF (red), MXene (green), and Fe SAS- MXene electrodes (blue).

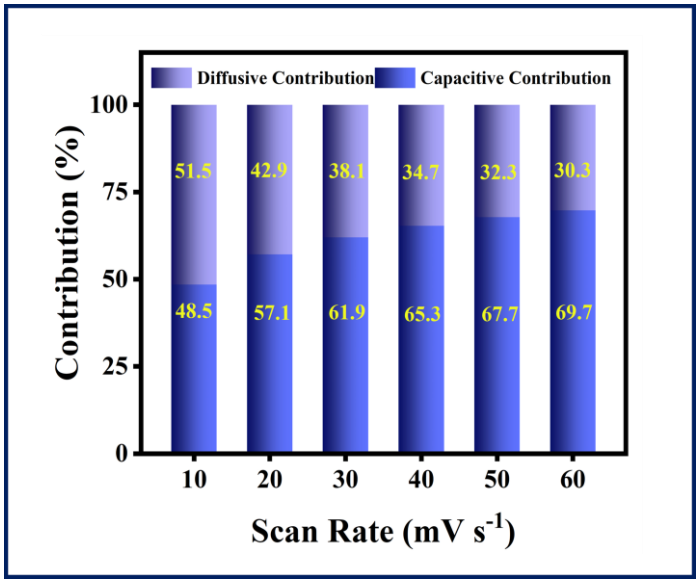

Fig. S17. Diffusive and capacitive contribution in percentage (%) of the Fe SAS-MXene.

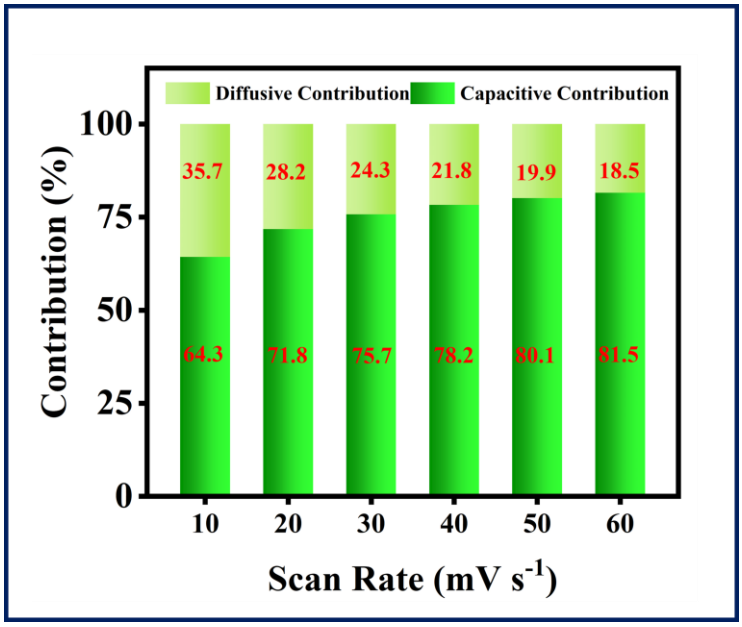

Fig. S18. Diffusive and capacitive contribution in percentage (%) of the MXene.

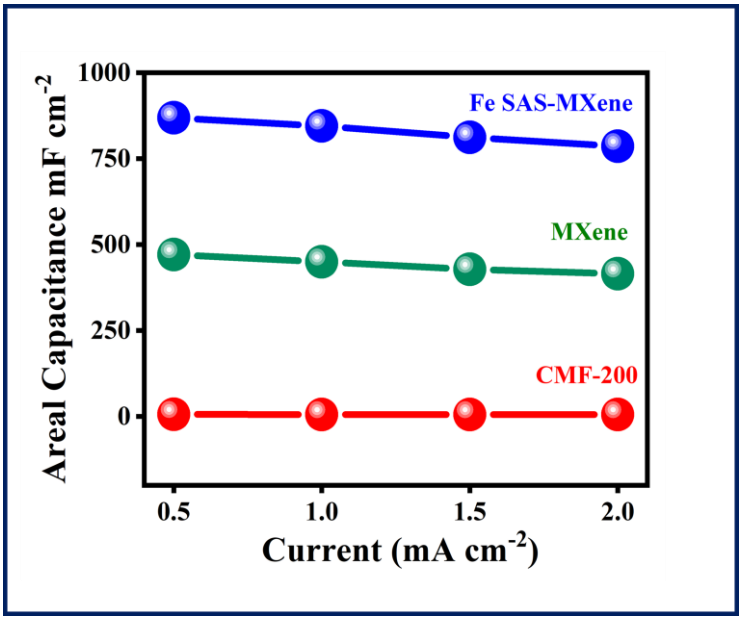

Fig. S19. Capacitance comparison plot of all developed electrodes.

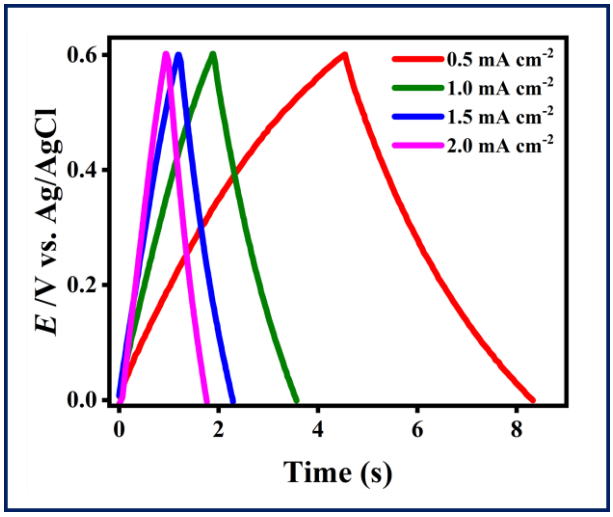

Fig. S20. GCD curves of CMF-200 measured at different applied current densities, starting from 0.5 to 2.0 mA cm^{-2} in 1.0 M H_2SO_4.

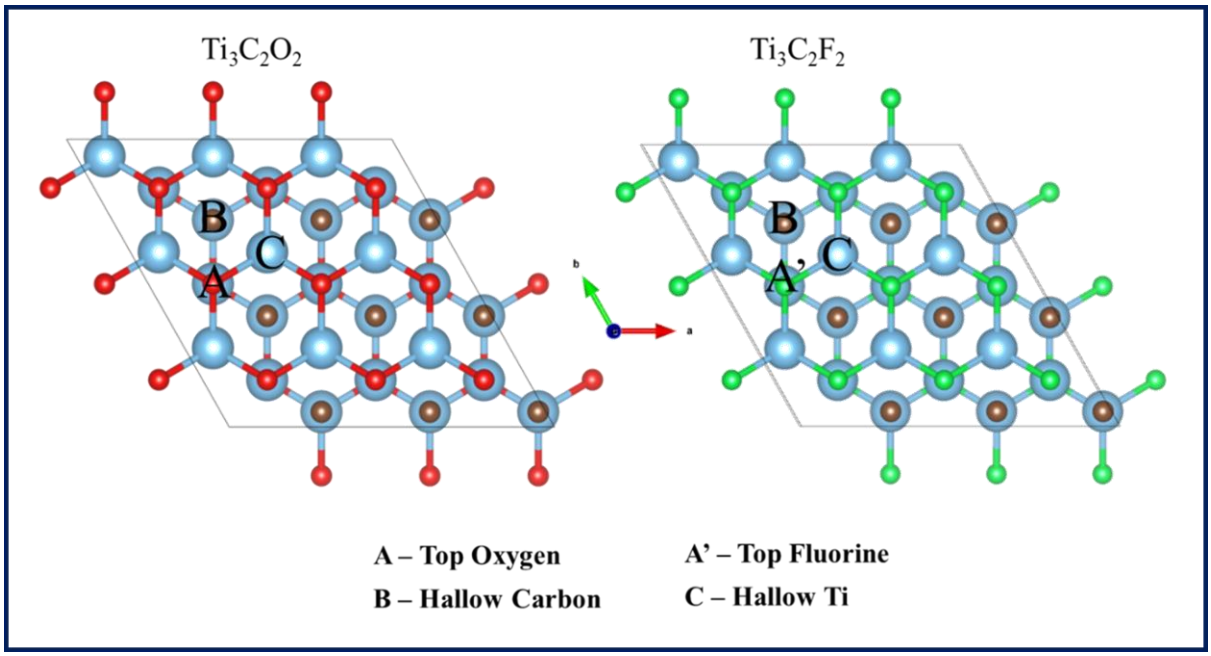

Fig. S21. Different adsorption sites (A, B, and C) for Fe on O- and F-terminated Ti_3C_2 MXene surfaces.

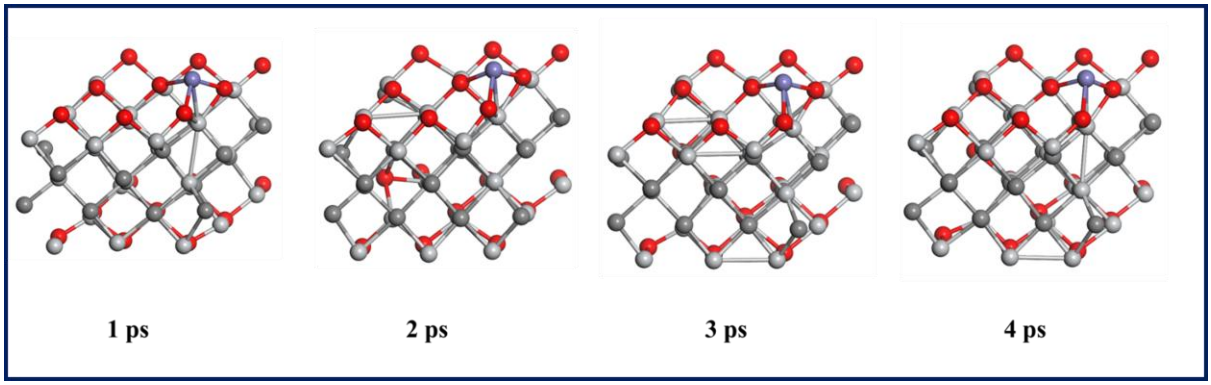

Fig. S22. AIMD snapshots of Fe atoms embedded in the Ti_3C_2 MXene at [temperature 300 K], showing the structural evolution and stability over the simulation time.

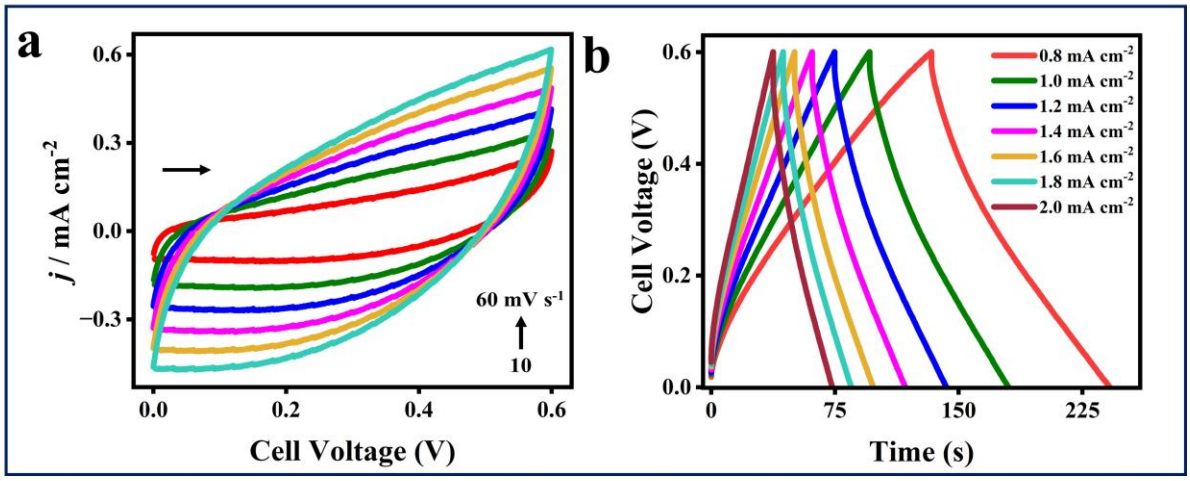

Fig. S23. CV curves **(a),** and GCD curves of the MSCs recorded at different scan rates (10 - 0 mV s^{-1}) and varied applied current densities, starting from 0.8 to 2.0 mA cm^{-2} **(b)**.

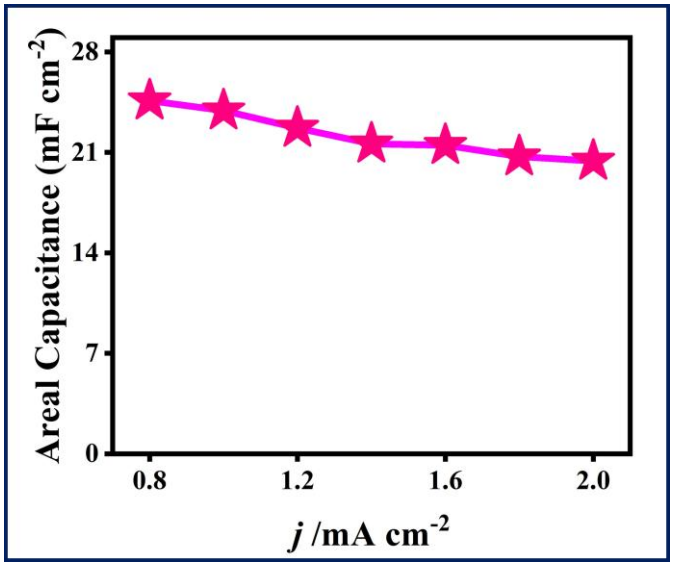

Fig. S24. Areal capacitance comparison (different applied current densities) of Fe SAS-MXene -MSCs electrodes**.**

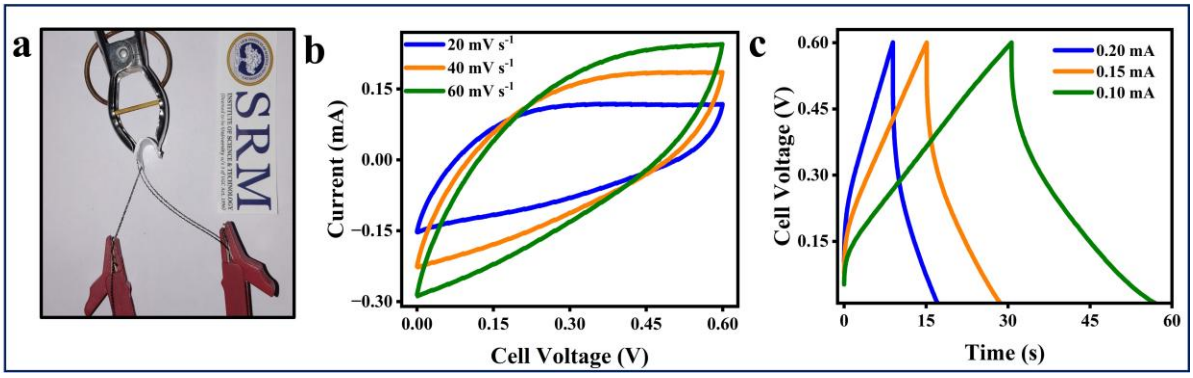

Fig. S25. Photograph (a), CV (b), and GCD (c) curves of the Fe SAS-MXene -MSCs device 50 % folded.

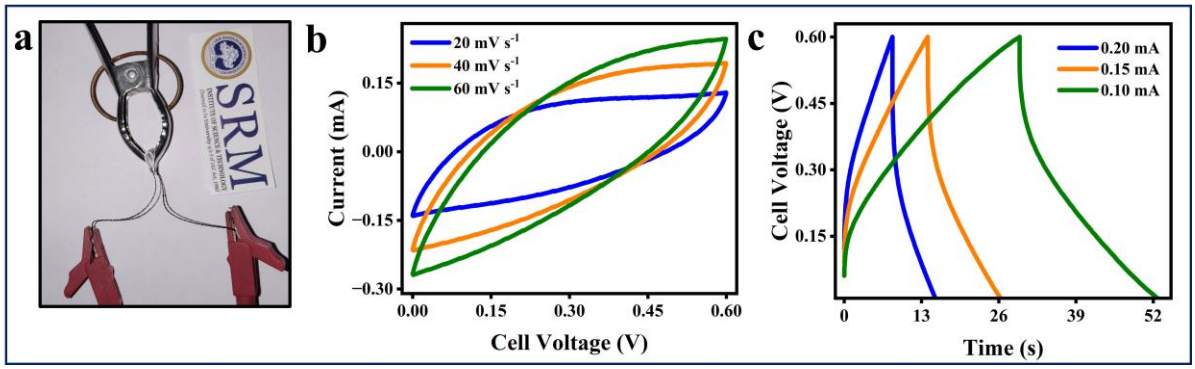

Fig. S26. Photograph (a), CV (b), and GCD (c) curves of Fe SAS-MXene -MSCs device 100 % folded.

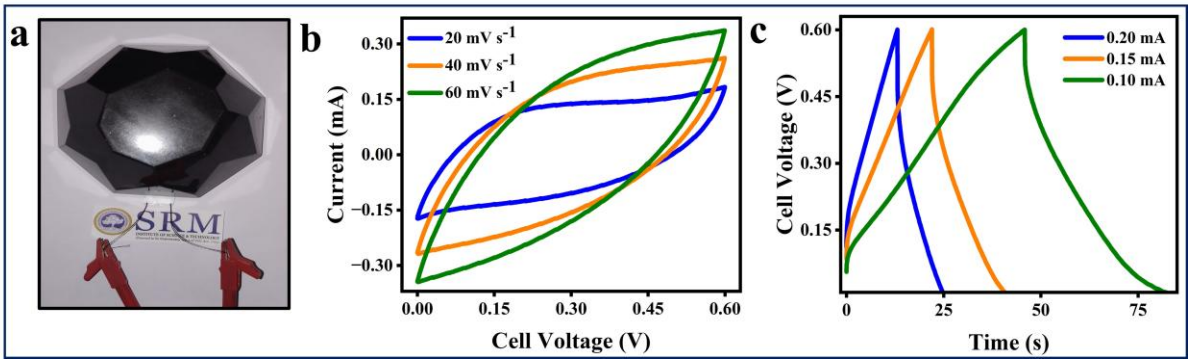

Fig. S27. Photograph (a), CV (b), and GCD (c) curves of Fe SAS-MXene -MSCs device under-weight stress.

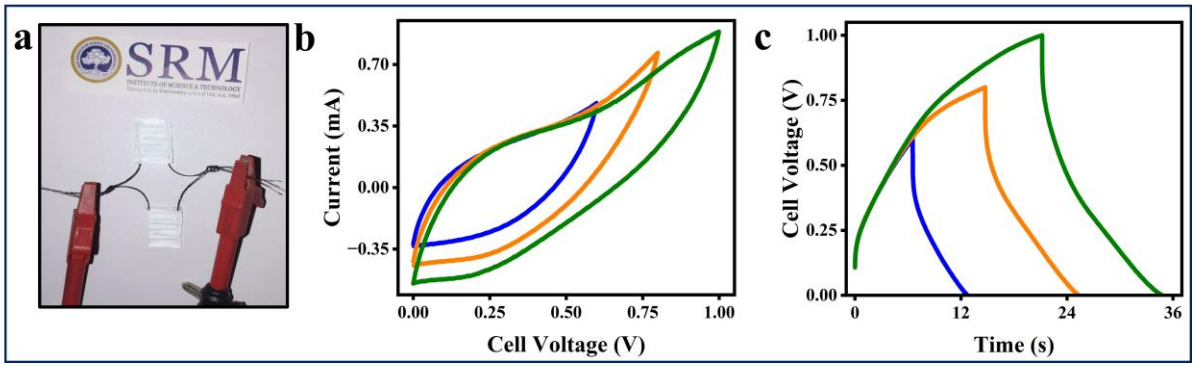

Fig. S28. Photograph (**a**), CV **(b),** and GCD **(c)** curves of Fe SAS-MXene -MSCs device, parallelly connected.

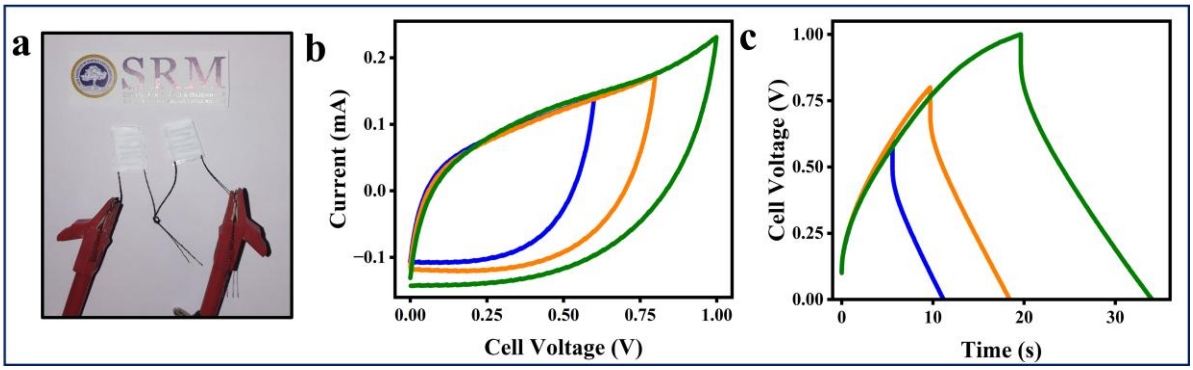

Fig. S29. Photograph **(a)**, CV **(b),** and GCD **(c)** curves of the Fe SAS-MXene -MSCs device serially connected.

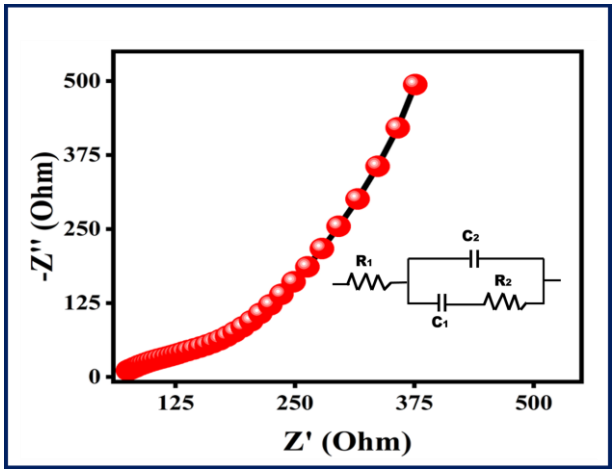

Fig. S30. EIS spectra for Fe SAS-MXene- MSCs; inset: the fitted electronic equivalent circuit.

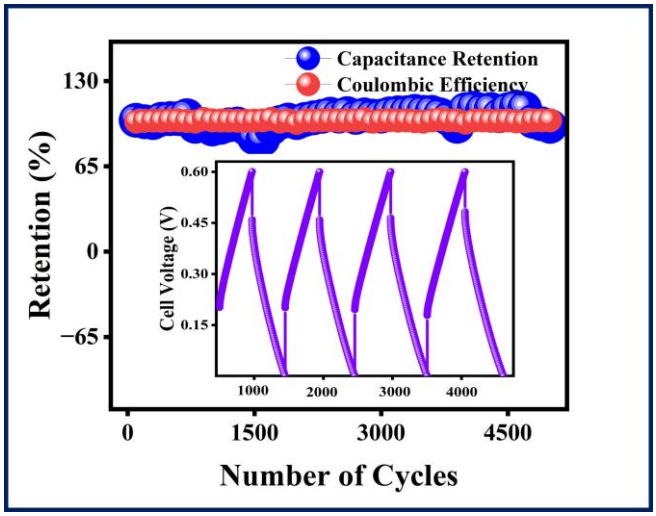

Fig. S31. Stability test of the MSCs; Capacitance retention (blue curve) and Coulombic efficiency (red curve); inset: GCD cycles.

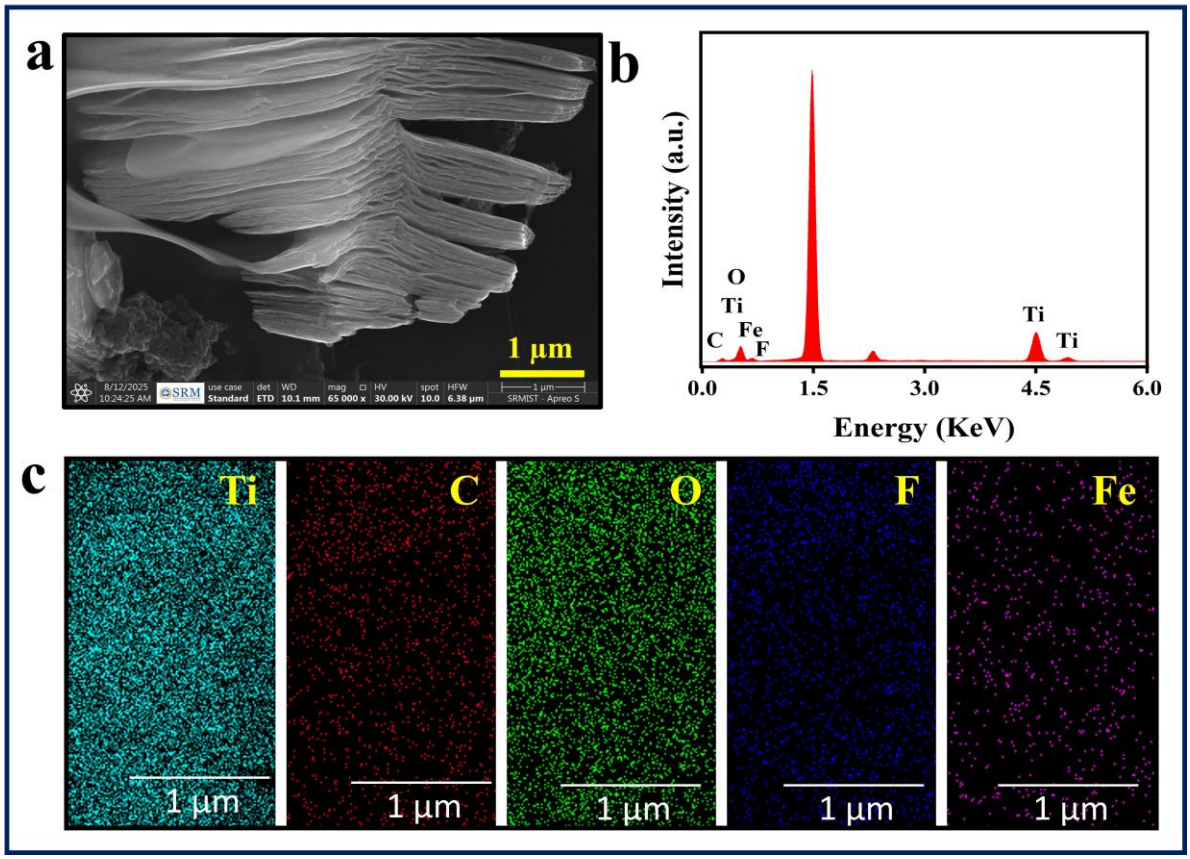

Fig. S32. SEM image **(a),** EDX spectra **(b),** and elemental mapping (Ti, C, O, F, and Fe) of Fe SAS-MXene after 5000 charging and discharging cycles **(c)**.

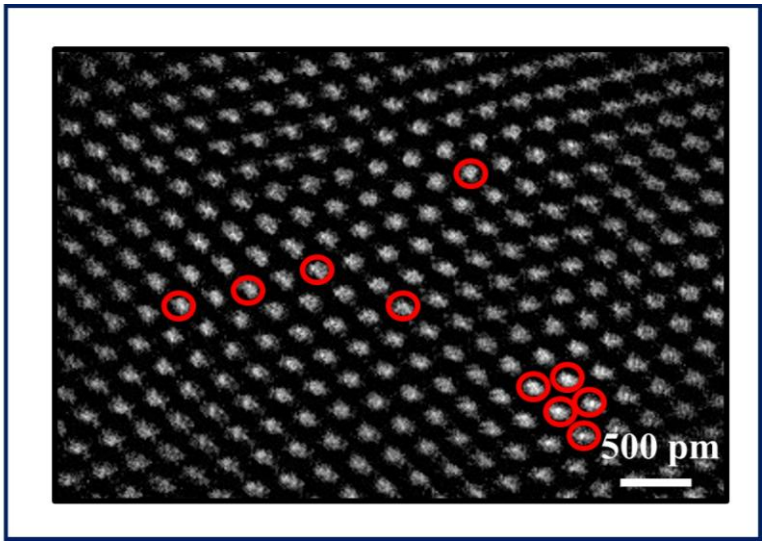

Fig. S33. TEM image of Fe SAS-MXene after 5000 charging and discharging cycles.

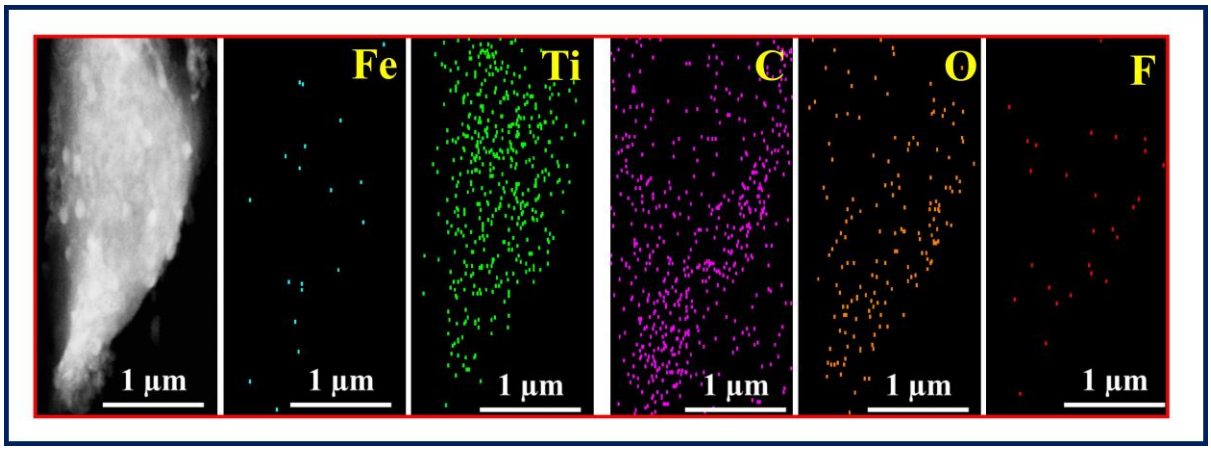

Fig. S34. Elemental mapping (Fe, Ti, C, O, and F) of the Fe SAS-MXene electrodes after stability.

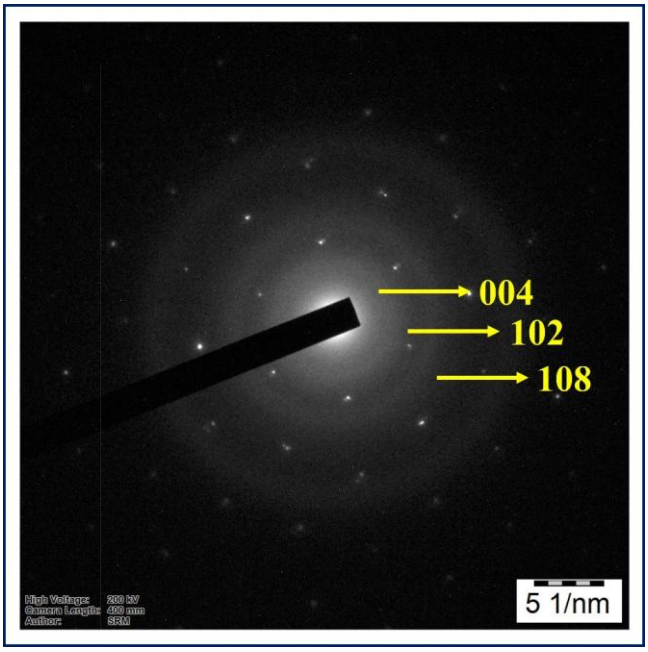

Fig. S35. SAED pattern of the Fe SAS-MXene electrode after 5000 charging and discharging cycles.

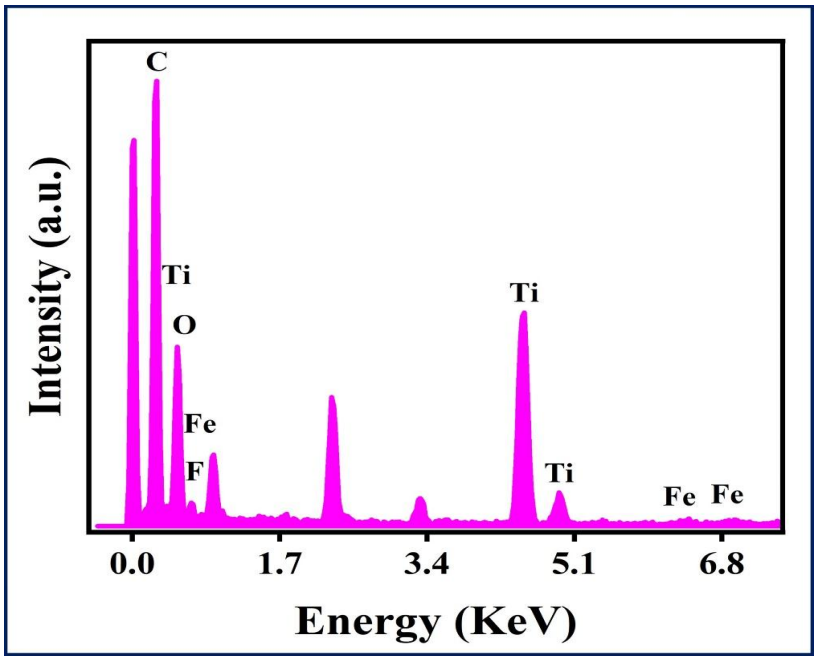

Fig. S36. EDX spectra of the Fe SAS-MXene electrode after 5000 charging and discharging cycles.

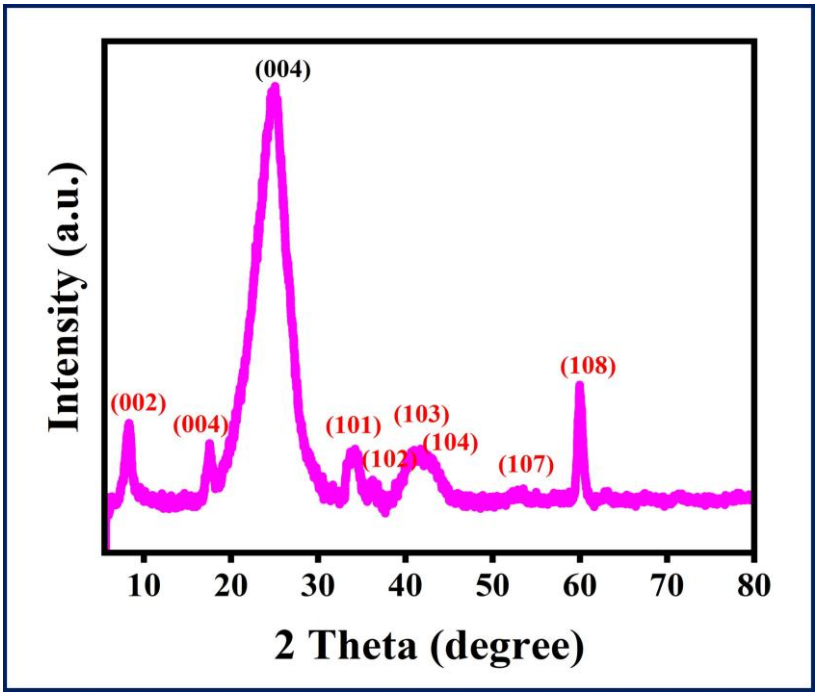

Fig. S37. XRD pattern of the Fe SAS-MXene electrode after 5000 charging and discharging cycles.

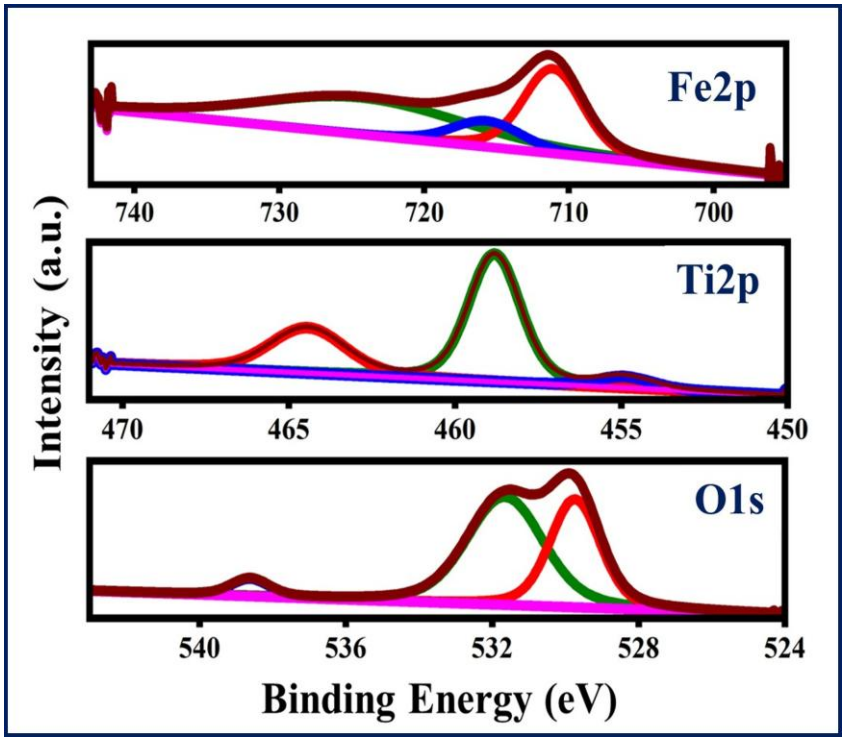

Fig. S38. HRXPS spectra of Fe 2p, Ti 2p, and O 1s of Fe SAS-MXene electrode after 5000 charging and discharging cycles

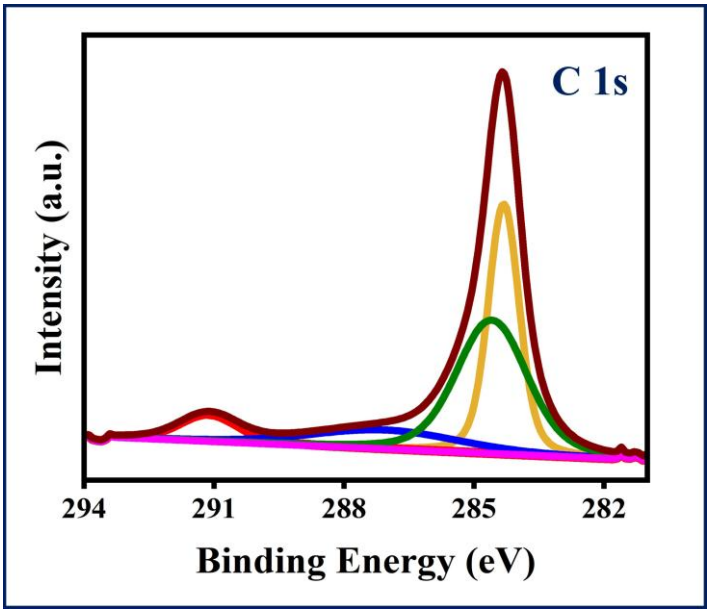

Fig. S39. HRXPS C1s spectra of Fe SAS-MXene electrodes after 5000 charging and discharging cycles.

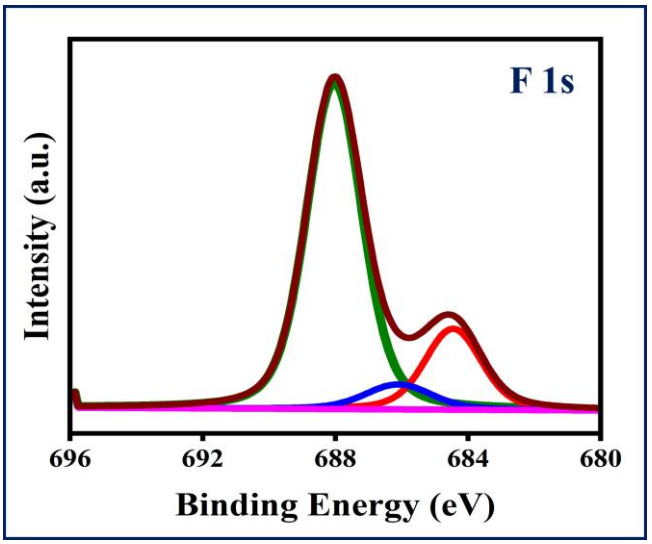

Fig. S40. HRXPS F1s spectra of Fe SAS-MXene electrodes after 5000 charging and discharging cycles.

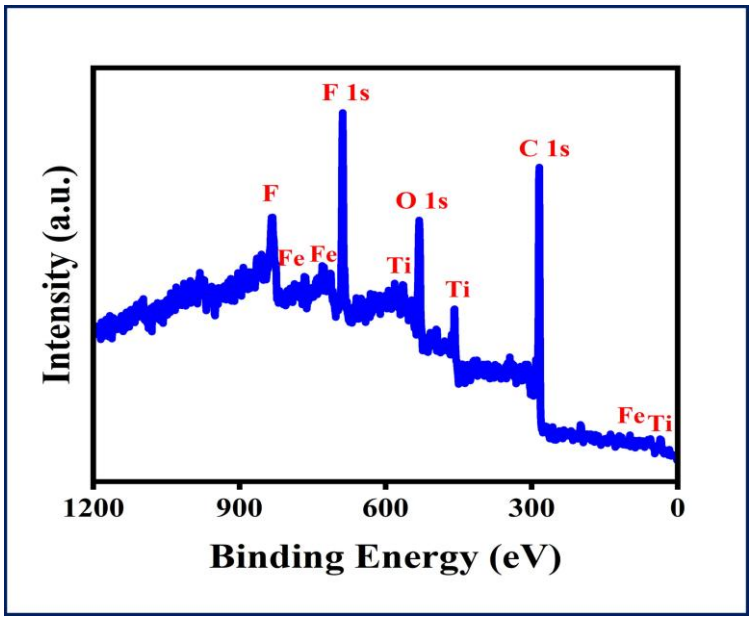

Fig. S41. HRXPS survey spectra of Fe SAS-MXene electrodes after 5000 charging and discharging cycles.

References:

1 M. V. Inbaraj and G. Maduraiveeran, *Chem. Commun.*, 2025, **61**, 5459–5462.

2 Y.-J. Gu, W. Wen and J.-M. Wu, *J. Mater. Chem. A*, 2018, **6**, 21078–21086.

3 A. Sharma, A. Patra, K. Namsheer, P. Mane, B. Chakraborty and C. S. Rout, *J. Mater. Sci.*, 2021, **56**, 20008–20025.

4 N. Kurra, C. Xia, M. N. Hedhili and H. N. Alshareef, *Chem. Commun.*, 2015, **51**, 10494–10497.

5 C. Gunasekaran, G. Shanmugam, S. Sreedhar and M. Venkatesan, *Electrochim. Acta*, 2025, **516**, 145725.

6 G. Zhou, X. Liu, C. Liu, Z. Li, C. Liu, X. Shi, Z. Li, C. Mei and M.-C. Li, *J. Mater. Chem. A*, 2024, **12**, 3734–3744.

7 J. P. Perdew, K. Burke and M. Ernzerhof, *Phys. Rev. Lett.*, 1996, **77**, 3865–3868.

8 S. Grimme, J. Antony, S. Ehrlich and H. Krieg, *J. Chem. Phys.*, 2010, **132**, 154104.

9 S. Goedecker, M. Teter and J. Hutter, *Phys. Rev. B*, 1996, **54**, 1703–1710.

10 R. Liu, Y. Gao, Y. Yang and Y. Liu, *J. Control Sci. Eng.*, 2015, **2015**, 349186.

11 S. Kamalakannan, M. Prakash, M. M. Al-Mogren, G. Chambaud and M. Hochlaf, *J. Phys. Chem. C*, 2019, **123**, 15087–15098.

12 H. Xue, P.-H. Huang, L.-L. Lai, Y. Su, A. Strömberg, G. Cao, Y. Fan, S. Khartsev, M. Göthelid, Y.-T. Sun, J. Weissenrieder, K. B. Gylfason, F. Niklaus and J. Li, *Carbon Energy*, 2024, **6**, e442.

13 N. Kurra, B. Ahmed, Y. Gogotsi and H. N. Alshareef, *Adv. Energy Mater.*, 2016, **6**, 1601372.

14 Y. Yue, N. Liu, Y. Ma, S. Wang, W. Liu, C. Luo, H. Zhang, F. Cheng, J. Rao, X. Hu, J. Su and Y. Gao, *ACS Nano*, 2018, **12**, 4224–4232.

15 S. Guo, R. Zhu, J. Chen, W. Liu, Y. Zhang, J. Li and H. Li, *Microsystems Nanoeng.*, 2024, **10**, 89.

16 Q. Jiang, C. Wu, Z. Wang, A. C. Wang, J.-H. He, Z. L. Wang and H. N. Alshareef, *Nano Energy*, 2018, **45**, 266–272.

17 Y. Zhu, Z. Ni, J. Gao, D. Zhang, S. Wang and J. Zhao, *J. Phys. Chem. Solids*, 2023, **183**, 111619.

18 Z. Cao, Y. Wu, L. Jin, X. Li, D. Qian and H. Hu, *Adv. Funct. Mater.*, 2025, **n/a**, e26006.

19 J. Zhang, K. Wang, P. Lu, J. Gao, Z. Cao, F. Mo, D. Ho, B. Li and H. Hu, *Adv. Funct. Mater.*, 2024, **34**, 2310775.